Chapter 54
Quantifying the Key Role of Slope Material Peak Strength – Using Discrete Element Simulations

Katrin Huhn, Frank Strozyk, and Ingo Kock

Abstract This study investigates how progressive oversteepening and fault kinematics impact on slope failure initiation and subsequent landsliding along subsiding basin flanks using 2D DEM simulations. We use large assemblages of granular particles to simulate the deformation behaviour of slope sediments with varying peak strength. Sediments with high peak strength deform preferentially on major faults and produce a stepped topography and a stable slope in the long-term. Mass failures in these sediments occur as large, compact slides of short run out. In contrast, slopes with lower peak strength deform diffusely and present large numbers of faults that fail frequently and maintain the slope at its critical angle of inclination. The resulting slope topography is smoother and laterally more elongated. These differences in mass movements are governed by (i) characteristic fault patterns, and (ii) repeated oversteepening during ongoing basin subsidence, which is an important prerequisite for failure initiation. Our experiments indicate quantitatively that the failure distribution, dimension, and transport mechanism, as well as the recurrence rate of landslides are essentially controlled by the peak strength of the failed material.

54.1 Introduction

The evolution of sedimentary basins is often associated with slope failure events occurring along steepening basin flanks due to ongoing basin subsidence. Hence, tectonic movements and oversteepening exert an important control on the

K. Huhn (✉)
MARUM – Center for Marine Environmental Sciences, Universität of Bremen, Leobener Str., 28359 Bremen, Germany
e-mail: khuhn@marum.de

F. Strozyk
RWTH Aachen, Geologisches Institut, Wüllnerstr. 2, 52062 Aachen, Germany

I. Kock
GRSmbH, Schwertnergasse 1, 50667 Köln, Germany

G. Lamarche et al. (eds.), *Submarine Mass Movements and their Consequences*, Advances in Natural and Technological Hazards Research 41,
DOI 10.1007/978-3-319-20979-1_54

occurrence of gravitational mass movements (Hampton and Lee 1996). Although other mechanisms, e.g. transients in excess pore pressure (Stegmann et al. 2007) or seismic loading (Biscontin and Pestana 2006), are generally proposed as major trigger of failure events, at least a small inclination is required to cause slope destabilisation. The critical inclination depends on sediment physical properties (Hampton and Lee 1996). Hence, in general terms tectonic oversteepening plays a major role in failure pre-condition whereas sediment mechanical attributes exert an important constraint on slope failure development (Lee et al. 2007). However, the interplay between sediment physical properties and localisation and transport mechanism of landslides is still not fully quantitatively understood.

The major aim of this study is to highlight the key role of sediment physical properties, particularly the peak strength of the failed material, on slope deformation, e.g. fault activity, failure events and topography evolution. Therefore, we test two end-member materials with contrasting peak strength: a sandy-like slope sediment with high strength (material-A), versus a muddy slope with lower strength (material-B). Tectonic movement is linked to landslide patterns along different sedimentary slopes by utilizing a numerical particle based simulation technique – the Discrete Element Method (DEM). We simulate the evolution of basin flanks resulting from ongoing subsidence along a single normal fault in a 2D experiment.

54.2 Theory and Model Configuration

54.2.1 The Discrete Element Method

The Discrete Element Method (DEM) is a numerical simulation technique based on the description of granular materials. In this study, we use the commercial Particle Flow Code *PFC2D* in 2-dimensions (Itasca, Inc. ® (Itasca 2004)) which utilizes the theory by Cundall and Strack (1979) (see also e.g. Morgan and Boettcher 1999).

The numerical 'slope sediments' are simulated by an assemblages of discrete, rigid, frictionally coupled, spherical particles which interact as common contact points in accordance to simple physical contact laws (Fig. 54.1a). As we are aiming to simulate a Mohr-Coulomb material, particle micro-properties, e.g. particles' density (ρ), coefficient of friction (μ_P) and shear and normal stiffnesses (k_S, k_N) have to be defined (Table 54.1). In addition, variations in peak strength are simulated by bonding of particles (via normal (B_N) and shear bond stiffnesses (B_S)).

Particles can be displaced in any direction forced by the given boundary conditions, while interacting and overlapping (ΔD) with their neighbours (Fig. 54.1a). Resulting forces (normal – F_N; shear – F_S) are calculated using simple physical laws. Subsequently, all forces acting on a single particle are summed up; and Newton's 2nd law is used to calculate the resulting particle displacement and the new particle position. Furthermore, shear forces are used to define if particles are gliding away. Hence, maximum shear forces are simulating the peak strength of the

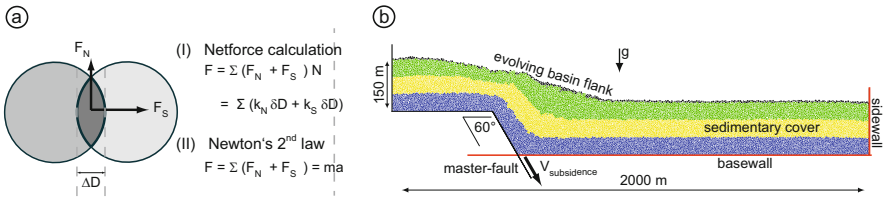

Fig. 54.1 (**a**) DEM principles of contact force calculation and displacement calculation, (**b**) basic model setup used to generate a 2D sedimentary slope simulating basin subsidence along a 60° master-normal fault. The models are performed with 0.1 [m/s] base-wall off-set until the total vertical off-set equals the 150-m-thickness of the particle ('sediment') assemblage. 'Sediment' cover is marked by coloured particles. Moving walls are marked in *red*

Table 54.1 Defined micro-(particle)-properties and calibrated macro-(material)-properties to simulate two slope sediment end-members

Micro-properties	**Material-A** ('**sand**')	**Material-B** ('**mud**')
Density ρ [kg/m^3]	2000.0	2000.0
Coefficient of particle friction μ_p	0.6	0.1
Particle stiffnesses k_N k_S [N/m^2]	1.0×10^{10}	1.0×10^{10}
Bond stiffnesses B_N; B_S [N/m^2]	1.25×10^5	1×10^1
Wall stiffness k_N; k_S [N/m^2]	1×10^9	1×10^9
Coefficient of wall friction μ_{wall}	0.6	0.1
Macro-properties		
Coefficient of friction μ_{bulk}	0.37	0.18
Peak strength τ [kPa]	49.8	4.64

material. So a progressive breaking of contacts to discrete planes reproduces fractures and faults in nature. Besides, the micro-particle-properties of a single particle do not correspond to the bulk macro-properties of the entire particle assemblage (e.g. Kock and Huhn 2007). Hence, the values of the bulk material properties have to be defined to simulate natural material behaviour.

54.2.2 Numerical 'Slope Sediments'

As the micro-properties in the DEM do not correspond with the macro-properties of the particle assemblage, e.g., we utilize numerical direct shear tests (e.g. Kock and Huhn 2007), and standard 2-D biaxial shear tests (Itasca 2004) to calibrate micro-properties of the particle assemblage to reproduce the deformation behaviour and mechanical macro-properties in accordance to natural slope materials.

In order to test the key role of material strength on failure events, we designed two numerical sediment end-members: (A) sandy 'sediments' and (B) mud-rich 'sediments' (Table 54.1). The physical and mechanical behaviour of material-A simulates typical siliciclastic sediment with higher strength as observed e.g. in the northern Gulf of Mexico (Balsam and Beeson 2003) and the slope off Norway (Jackson et al. 2008). In contrast, material-B resembles muddy slope sediments with lower strength, e.g. from the northern Cretan margin (Strozyk et al. 2010).

54.2.3 Model Configuration

We generate a rectangular fixed box model of 2000 m length and 200 m height to simulate a flat basin. All walls are defined as impermeable and stiff boundaries (Fig. 54.1b). Approximately 22,000 particles with a Gaussian particle size distribution and diameters between 1 and 3 m are generated in this fixed box. These particles settle down under gravity generating the 150-m-thick undeformed basin 'sediment' layer. 'Sediment' thickness and particle resolution enable modelling of slide events of meter to several tens of meters thickness in a reasonable calculation time.

Basin subsidence is performed by a continuous downward motion of two thirds of the box bottom wall along a 60° inclined master-fault (Fig. 54.1b). Movement along this master-fault simulates basin flank evolution. The angle of master-fault inclination represents the average orientation of brittle material failure in nature. The basin wall subsides until the total vertical off-set equals the initial material thickness of 150 m (Fig. 54.1b). Subsidence velocity was dynamically chosen to ensure a force and momentum equilibrium at each calculation time (Cundall and Strack 1979); and low strain rates are ensured.

During each experimental run, particle configuration as well as forces are saved every 0.7–1 m subsidence. These data are processed to gain geological interpretable data, e.g. fault zones, fault kinematics and mass transfer patterns (Figs. 54.2 and 54.3).

54.3 Results and Interpretation

In all experiments, numerous fault zones evolve, basin slope flanks oversteep and gravitational mass movements occur in consequence of basin subsidence, outlining a highly deformed slope segment (Fig. 54.2). In particular, a tectonically inactive footwall and hanging wall could be identified which are separated by major faults embedding a highly deformed slope segment. This segment is always characterized by near-surface mass movements and shows further segmentation into an upper, extension-dominated, and a lower, compression-dominated slope. However, slope evolution differ significantly according to slope type, especially material strength.

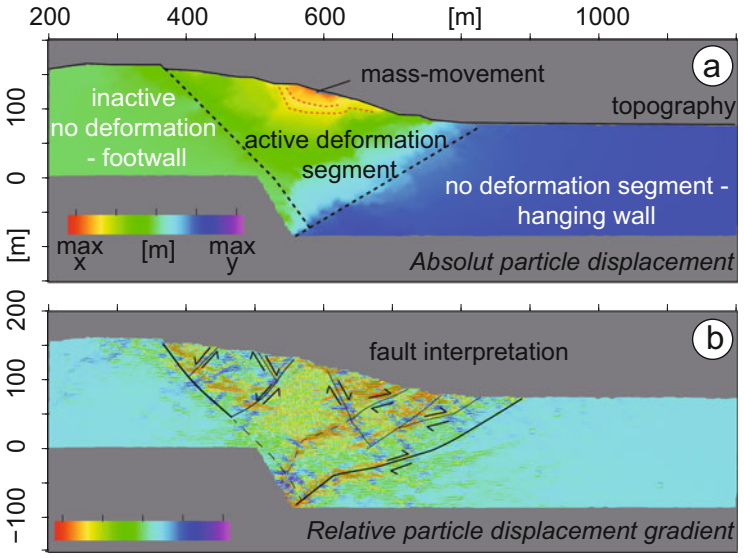

Fig. 54.2 Example of data visualization styles within a calculation step of 0.7 m subsidence: (**a**) absolute particle displacement plot depicts three deformation segments and gravitational mass transport along distinct slid masses, (**b**) relative displacement field calculated from offset between single neighbouring particles enables to identify and track fault evolution. *Black* indicate active faults. *Dashed lines* mark older faults only active at initial subsidence

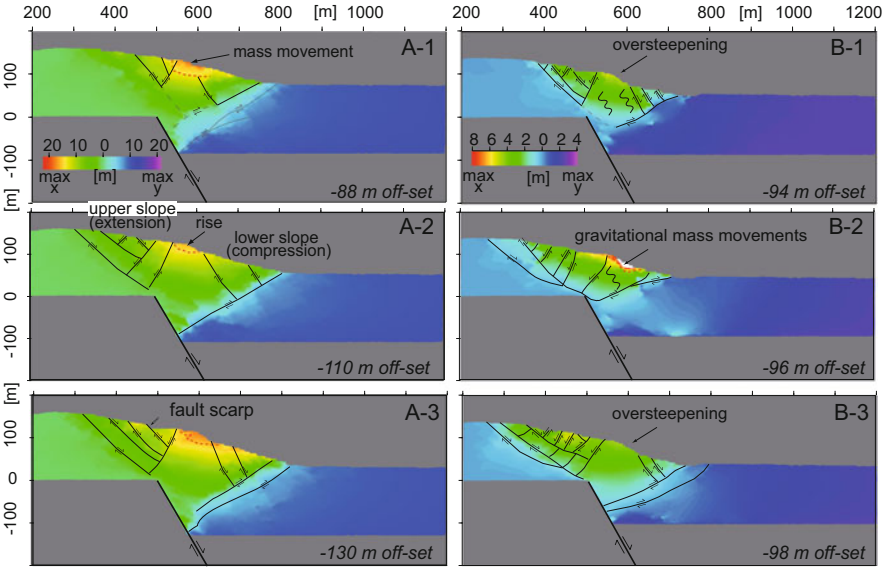

Fig. 54.3 Time series of incremental particle displacement plots for 20-m basin subsidence for material-A (A1-3) and material-B (B1-3). *Black lines* indicate potential faults; which were at least for a short term active, but accumulating not necessarily significant offsets. *Yellow* to *orange* colours indicate the occurrence of near-surface mass movements; also marked by *red dotted line*

54.3.1 High Peak Strength, 'Sandy' Slope Covers (Material-A)

(*i*) *Evolution of deformation segments and fault system*: The active deformation segment evolves immediately after basin subsidence. After 150 m subsidence, this segment exhibits a width of 600 m. This lateral extension is primarily caused by a basin-ward migration of the large-scaled, antithetic thrusts which establish towards the foot of the slope (Fig. 54.3a). Furthermore, the internal deformation of the active slope segment is mainly controlled by numerous normal faults, which often produce steep fault scarps at the surface (Fig. 54.3A-2). Sub-ordinated, mostly antithetic, minor faults occur only over short time-periods. Hence, extensional behaviour is the most prominent deformation mechanism, represented by extensional sub-segments of 10–50 m width. Compression is only observed in a narrow range at the basin-side of the active segment where slope material is overthrusting the undeformed hanging wall (Fig. 54.3A-3). This indicates that material-A deforms preferentially along major faults, while internal deformation of the embedded sub-segments is low. (*ii*) *Slope topography*: A typical tripartite evolves: the nearly flat hanging and footwall inactive segments as well as the embedded steeper, even deforming slope (Fig. 54.3A). Slope angles increase continuously until a typical gently dipping upper (α_{upper} = 4–8°) and steeper lower slope (α_{lower} = 15–28°) could be identified after 90 m subsidence. This change in slope taper marked by a rise correlates always with the lower edge of the master fault. Hence, the rise moves continuously basin-ward simultaneously to basin subsidence. Furthermore, based on long-term activity of major normal faults and high stability of the small-scaled extensional sub-segments, the upper slope is characterized by an alternation of smoother topography of flat sub-segments and areas of highest slope gradients correlating with fault scarps (~35°; Fig. 54.3-A3). Thus, the outcropping scarps of major faults lead to a steep, stepped topography and irregular morphology of the upper, extension-dominated slope (Fig. 54.3A).

(*iii*) *Gravitational mass movement pattern*: Sliding always occurs at the transition between upper and lower slope (Fig. 54.3). In general, headwalls of slides generate steep normal fault scarps outcropping at the upper slope. The destabilized masses occur as deep-incised, wedge-shaped, compact bodies with partial downward concave shear planes. Hence, mass transport is dominated by low internal deformation and short runout. In addition, sliding events show a recurrence with at max. one event per 20-m subsidence. In addition, failure alternates with periods of slope stability. The dimension of the described mass movements is linked to the stage of basin subsidence. So, as slope failure headwalls migrate in footwall direction (re-)activating younger normal faults, failure events mobilize larger 'sediment' portions. The largest slope failure event of >200 m width and about 50 m in thickness could be observed in the final model stages.

54.3.2 Low Peak Strength, 'Muddy' Slope Covers (Material-B)

(*i*) *Evolution of deformation segments and fault system*: Deformation segments establish immediately and the active slope reaches its largest lateral extension of ~650 m after more than 100 m basin subsidence (Fig. 54.3B-3). Again, major, long-term active normal faults and thrust faults continuously define the outer limits of the active segment. However, while the thrust faults are more or less static in position, they vary in number and activity. Internal deformation of these slope segment tends to be dominated by dense sets of short-term (i.e. <2 m subsidence intervals), active normal and antithetic thrust faults (Fig. 54.3B-2). This overall more diffuse and widespread deformation strongly contrasts with the establishment of less-deformed sub-segments in model-A. (*ii*) *Slope topography*: Surface topography is similar to model-A, but with slightly lower-inclination ($\alpha_{upper} = 4–6°$ and $\alpha_{lower} = 14–18°$), and a well-defined rise is not observable. Furthermore, slope angle transitions at both active-inactive-segment boundaries are smoother. Hence, the entire slope maintains a smoother topography. Nevertheless, the upper slope periodically develops faults scarps due to ongoing normal faulting. (*iii*) *Gravitational mass movement pattern*: After a basin subsidence of 100 m, mass movements occur almost continuously along the different slope segments. However, the size of single events decrease, while their number and the transport distance increase. Slides with a maximum thickness of 10–20 m and 20–50 m in length with transport distances of >200 m occur (Fig. 54.3B-2). Their mean recurrence rate is about 1–2 events per 4-m subsidence interval. Further, some of the detected mass-movement events correlate to a temporary activation of minor low-angle normal faults at the continental rise similar to model-A. However, we observe that oversteepening is immediately balanced by a high number of mass movements. This contrasts strongly with the long-term stability of sub-segments in model-A.

54.4 Summary and Conclusions

In this study, we have shown that the long-term evolution of extensional basin flanks (particularly the associated fault pattern and mass movements) is strongly predisposed by the mechanical behavior of the slope sediments. This modelling approach enables investigation and testing of common hypotheses and conceptual models (e.g., Hampton and Lee 1996; Locat and Lee 2002). Nevertheless, we are aware that there are numerous differences between natural slopes and models. However, our very simplified model already demonstrates the key role of the peak strength of the slope sediments and enables a deeper insight into the controlling factors of failure kinematics. Comparing our observations and interpretations, we conclude that:

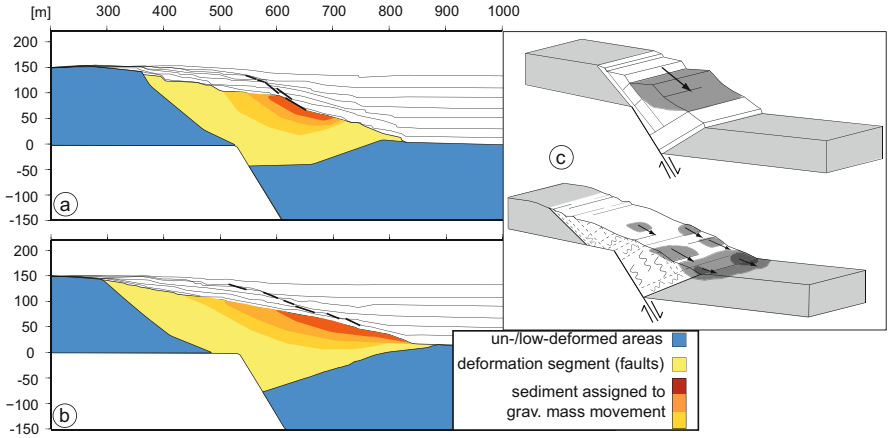

Fig. 54.4 The displacement that occurs from 150 m basin subsidence ((**a**) material-A; (**b**) material-B). Slope topography evolution is shown in 20-m subsidence intervals. *Thicker black lines* mark over steepened slopes. (**c**) Conceptual sketches for extensional basin slopes bearing in a high strength (*top*) vs. a low strength sedimentary cover (*bottom*)

- The activation and location of larger normal, slope-parallel faults are a limiting factor for the occurrence as well as the dimension, location, and the failure mechanism of slope instability in high strength sedimentary slopes. In this case, normal faults position and control the development of slide headwalls due to ongoing basin subsidence. Hence, stresses from the tectonic movement are accommodated by single major faults, while the slope is stable about long periods of time, and only occasional collapses occur (Fig. 54.4). In summary, these kind of slope flanks will exhibit less frequent mass wasting events, whereas sediment destabilization migrates upslope towards younger normal faults resulting in larger thick slides. Consequently, due to their short runout, the overall slope shape remains compact with a steep, stepped topography.
- In contrast, gravitational mass movements on low strength slopes occur along the lower-inclined slope parts, where deformation is accommodated by a diffuse faulting. In this case, material tends to fail more frequently along the entire portion of the slope but involves less material over larger run-outs. The high number of near-surface mass movements provides taper adjustment on one hand, and a high sediment supply to the slope foot region on the other hand which is associated to compressional deformation at the lower slope.

Acknowledgments This work has been funded by the DFG – MARUM. We gratefully acknowledge the constructive reviews by Dr Gian Andrea Pini and Dr Roger Urgeles. We also wish to thank Lina Podszun for her help with the figures.

References

Balsam WL, Beeson JP (2003) Sea-floor sediment distribution in the Gulf of Mexico. Deep-Sea Res 50:1421–1444

Biscontin G, Pestana JM (2006) Factors affecting seismic response of submarine slopes. Nat Hazards Earth Syst Sci 6:97–107

Cundall PA, Strack ODL (1979) A discrete numerical method for granular assemblies. Geotechnique 29:47–65

Hampton MA, Lee HJ (1996) Submarine landslides. doi:10.1029/96RG03287

Itasca Consulting Group (2004) Particle flow code in 2-D (PFC-2D) user's manual. Version 3.0

Jackson CAL, Barber GP, Martinsen OJ (2008) Submarine slope morphology as a control on the development of sand-rich turbidite depositional systems. Mar Petrol Geol 25:663–680

Kock I, Huhn K (2007) Numerical investigation of localization and micromechanics in a stratified soil specimen. J Struct Geo 29:1679–1694. doi:10.1016/j_jsg.2007.07.013

Lee HJ, Locat J, Desgagnes P et al (2007) Submarine mass movements on continental margins. In: Nittrouer CA et al (eds) Continental margin sedimentation. Blackwell, Oxford, pp 213–274

Locat J, Lee HJ (2002) Submarine landslides: advances and challenges. Can Geo J 39:193–212

Morgan JK, Boettcher MS (1999) Numerical simulations of granular shear zones using the distinct element method. J Geophys Res 104:2,703–2,719

Stegmann S, Strasser M, Anselmetti F, Kopf A (2007) Geotechnical in situ characterization of subaquatic slopes. Geophys Res Lett 34:L07607. doi:10.1029/2006GL029122

Strozyk F, Strasser M, Krastel S, Meyer M, Huhn K (2010) Reconstruction of retreating mass wasting in response to progressive slope steepening of the northeastern Cretan margin, eastern Mediterranean. Mar Geol 271(1–2):44–54